Estimation of raindrop size distribution and rain rate with infrared surveillance camera in dark conditions

Jinwook Lee[1], Jongyun Byun[1], Jongjin Baik[1], Changhyun Jun[1], Hyeon-Joon Kim[1]

[1]Department of Civil and Environmental Engineering, College of Engineering, Chung-Ang University, Seoul, 06974, South Korea

Correspondence to: Hyeon-Joon Kim (hjkim22@cau.ac.kr)

Abstract. This study estimated raindrop size distribution (DSD) and rainfall intensity with an infrared surveillance camera in dark conditions. Accordingly, rain streaks were extracted using a *k*-nearest neighbor (KNN)-based algorithm. The rainfall intensity was estimated using DSD based on physical optics analysis. The estimated DSD was verified using a disdrometer for the two rainfall events. The results are summarized as follows. First, a KNN-based algorithm can accurately recognize rain streaks from complex backgrounds captured by the camera. Second, the number concentration of raindrops obtained through closed-circuit television (CCTV) images had values between 100 $mm^{-1}m^{-3}$ and 1,000 $mm^{-1}m^{-3}$, the RMSE for the number concentration by CCTV and PARticle SIze and VELocity (PARSIVEL) was 72.3 $mm^{-1}m^{-3}$ and 131.6 $mm^{-1}m^{-3}$ in the 0.5 to 1.5 mm section. Third, maximum raindrop diameter and the number concentration of 1 mm or less produced similar results during the period with a high ratio of diameters of 3 mm or less. Finally, after comparing with the 15-min cumulative PARSIVEL rain rate, the mean absolute percent error (MAPE) was 49% and 23%, respectively. In addition, the differences according to rain rate can be found that the MAPE was 36% at a rain rate of less than 2 $mm\ h^{-1}$ and 80% at a rate above 2 $mm\ h^{-1}$. Also, when the rain rate was greater than 5 $mm\ h^{-1}$, MAPE was 33%. We confirmed the possibility of estimating an image-based DSD and rain rate obtained based on low-cost equipment during dark conditions.

1 Introduction

Precipitation data is vital in water resource management, hydrological research, and global change analysis. The primary means of measuring precipitation is to use a rain gauge (Allamano et al., 2015) to collect raindrops from the ground. Due to the restrictions on the installation environment of the rain gauge, it is difficult to understand the spatial rainfall distribution in mountains and urban areas (Kidd et al., 2017). Furthermore, the tipping-bucket-type rain gauge, which accounts for most rain gauges, has a discrete observation resolution (0.1 or 0.5 mm) for the discrete time-steps, producing uncertainty in temporal rainfall variation. For this reason, weighing gauges are nowadays used very often instead of tipping-bucket-type. the weighing gauge is a meteorological instrument used to observe and analyze various precipitation, including rainfall and snowfall. Also, the tipping bucket has a large error due to the observation time delay when the rainfall is less than 10 $mm\ h^{-1}$ compared to the

29 weighing gauge. However, when the observation time size is set to 10 to 15 minutes, the relative percentage error has a very

30 low value of -6.7~2.5%, resulting in high accuracy (Colli et al., 2014).

31   In contrast, it is possible to obtain spatial rainfall information on a global scale with remote sensing techniques (Famiglietti

32 et al., 2015). However, remote sensing techniques provide only indirect measurements that must be continuously calibrated

33 and verified through ground-level precipitation measurements (Michaelides et al., 2009). Recently, a disdrometer capable of

34 investigating the microphysics characteristics of rainfall has been used for observation instead of the traditional rainfall

35 observation instrument (Kathiravelu et al., 2016). However, these devices cannot be widely installed because of their high cost

36 and difficulty in accessing observational data. Consequently, a high-resolution and low-cost ground precipitation monitoring

37 network has not yet been established.

38   With the advent of the Internet of Things (IoT) era, using non-traditional sources is attractive for improving the spatio-

39 temporal scale of existing observation networks (McCabe et al., 2017). In recent years, such cases have been common in

40 rainfall observation. For example, there have been attempts to estimate rainfall using sensors to capture signal attenuation

41 characteristics in commercial cellular communication networks (Overeem et al., 2016), vehicle wipers (Raibei et al., 2013),

42 and smartphones (Guo et al., 2019). Furthermore, crowdsourcing information has been used to confirm the utility of estimating

43 regional rainfall (Haberlandt and Sester, 2010; Rabiei et al., 2016; Yang and Ng, 2017).

44   In a similar context, a surveillance camera is a sensor with high potential. Surveillance cameras are often referred to as

45 closed-circuit television (CCTV). Compared with other crowdsourcing methods, the visualization data of surveillance cameras

46 are highly intuitive (Guo et al., 2017). Therefore, they have been used in various fields (Cai et al., 2017; Nottle et al., 2017;

47 Hua, 2018). In Korea, public surveillance camera installations have been rapidly increasing, from approximately 150,000 in

48 2008 to 1.34 million in 2020—approximately a public CCTV camera per 0.07 km^2. Thus, the potential for precipitation

49 estimation using camera sensing is expected to be greater in Korea.

50   Recently, various studies have been conducted to estimate rainfall intensity using the rain streak image obtained from

51 surveillance camera videos. Many studies attempted to use artificial intelligence to capture changes in the image captured by

52 the camera when it rains (Zen et al., 2019; Avanzato and Beritelli, 2020; Wang et al., 2022). In contrast, some studies have

53 tried to estimate rainfall intensity using geometrical optics and photographic analyses. Typically, the rain streak layer is

54 separated from the raw image or video. A rain streak is the visual appearance of raindrops caused by visual persistence—

55 raindrops falling because of the blur phenomenon of raindrop movement from the camera's exposure time appears as streaks

56 on the image. Garg and Nayar (2005) made one of the first attempts to measure this rainfall.

57   Since then, many studies have been conducted to develop and improve efficient algorithms. Allamano et al. (2015)

58 proposed a framework to estimate the quantitative rainfall intensity using camera images based on physical optics from a

59 hydrological perspective. Dong et al. (2017) proposed a more robust approach to identifying raindrops and estimating rainfall

60 using a grayscale function, making grayscale subtraction nonlinear. Jiang et al. (2019) proposed an algorithm that decomposes

61 rain-containing images into rain streak layers and rainless background layers using convex optimization algorithms and

62 estimates instantaneous rainfall intensity through geometric optical analysis.

Some studies (e.g., Dong et al., 2017) have sought to estimate raindrop size distribution (DSD) using a surveillance camera. However, the existing studies have focused on the time when video can be captured with visible light. It is impossible to obtain input data without visible light using the existing image-based rainfall measurement method. Thus, these methodologies are only applicable in daytime conditions. However, when recording using infrared rays, it is possible to obtain a rainfall image even when there is no sunlight. No study has estimated the rain in dark conditions to our knowledge. Furthermore, most previous studies did not verify the estimated DSD using a disdrometer. In contrast, this study estimated DSD with an infrared surveillance camera in dark conditions, based on which rainfall intensity was also estimated. Rain streaks were extracted using a k-nearest neighbor (KNN)-based algorithm. The DSD was used to calculate rainfall intensity with physical optics analysis and verified using a PARticle SIze and VELocity (PARSIVEL) disdrometer (Löffler-Mang and Joss, 2000).

2 Methodology

2.1 Recording video containing rain streaks using infrared surveillance camera

The surveillance camera records video. The video looks continuous, but it is also composed of discrete still images, so-called frames. The frequency of recording frames (i.e., acquisition rate) is called frame per second (fps). In other words, fps is how many images are taken per second for recording video. Another important factor in video recording is exposure time. Exposure time, also called shutter speed, refers to the time the camera sensor is exposed to light to capture a single frame. The real raindrops are close to a circle, but in a single image, the raindrops look like a streak. This is because raindrops move at a high speed during the exposure time. Therefore, the raindrops that moved during the exposure time are visualized in the rain streaks in a single frame.

Fig. 1 shows an example of capturing a raindrop for a single frame. Here, only the raindrops near the point of focus are visible, and objects that are more than a certain distance appear invisible. That is, the point where the focus is best is called the focus plane, and there is a range in which it can be recognized that objects are focused before and after the focus plane. The closest plane that can be considered to be in focus is called the near-focus plane, and the farthest plane is called the far-focus plane. This range is generally called depth of field (DoF). Ultimately, the rainfall intensity can be estimated based on the volume and raindrops in the DoF.

In this study, an infrared surveillance camera was considered under dark conditions. Here, the dark condition refers to a condition in which raindrops cannot be captured by a general surveillance camera with visible light. Infrared cameras emit near-infrared rays through an infrared emitter and receive the reflected light from the objects. Accordingly, it has the advantage of being able to detect raindrops that are invisible to the human eye.
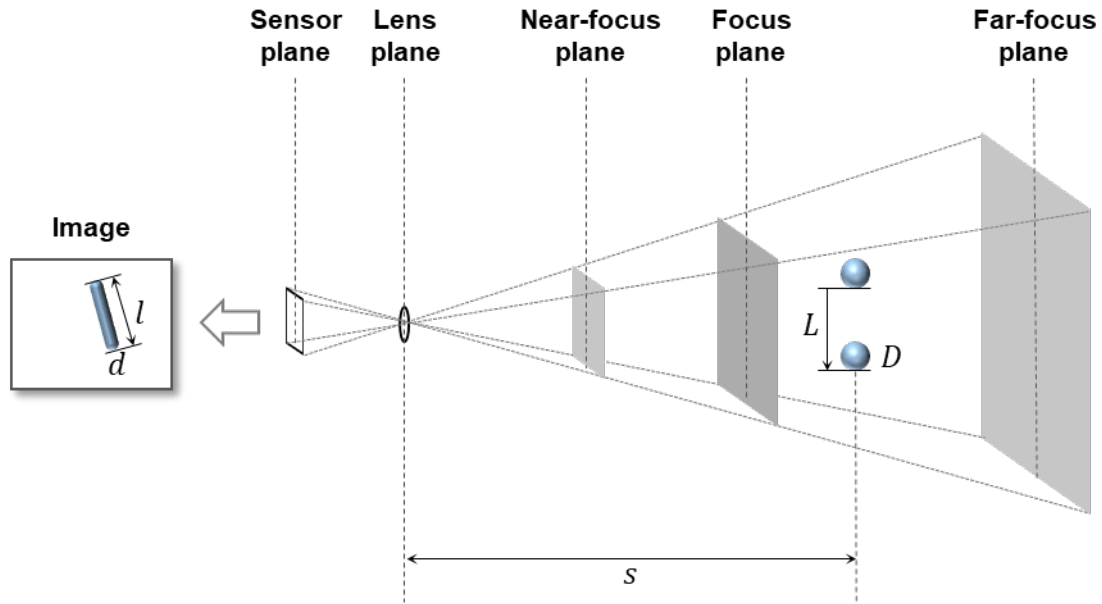
Figure 1: Schematic diagram of the photographed rain streak in the image and the movement of a raindrop during the exposure time.

2.2 Algorithm for identifying rain steaks and estimating DSD and rain rate

Image-based rainfall estimation can be divided into two processes: identifying rainfall streaks and estimating DSD. Fig. 2 illustrates these processes in a flowchart. Identifying rain streaks requires an algorithm that separates the moving rain streaks from the background layer. Next, in estimating DSD, raindrops are extracted from the image of the rain streaks, and the overall distribution is obtained.
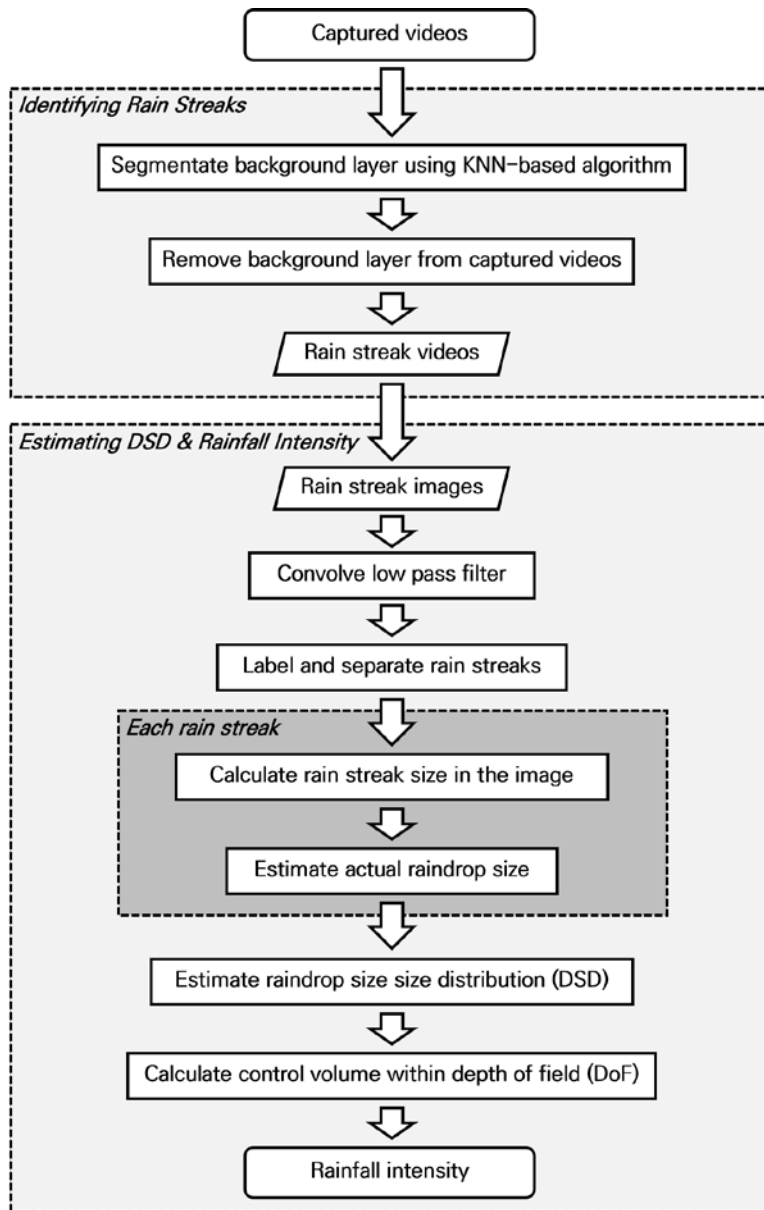
Figure 2: Flowchart of the methodology for estimating DSD and rainfall intensity.

Most existing algorithms aim to remove raindrops in images because raindrops are considered noise in object detection and tracking (Duthon et al., 2018). Such algorithms are categorized into multiple-image-based and single-image-based approaches (Jiang et al., 2018).

103   For example, Garg and Nayar (2007) classified the conditions in which the brightness difference between the previous
104   pixel and that of the next pixel exceeds a specific threshold over time, assuming that the background is fixed. Improved
105   algorithms were then developed considering the temporal correlation of raindrops (Kim et al., 2015) and chromatic properties
106   (Santhaseelan and Asari, 2015). Tripathi and Mukhopadhyay (2014) proposed a framework that removes rain that reduces the
107   visibility of the scene to improve the detection performance of image feature information. However, single-image-based
108   algorithms rely more on the properties of raindrops (Deng et al., 2018). The central idea of a single-image-based algorithm is
109   to decompose rain-containing images into rainless layers (Li et al., 2016; Deng et al., 2018; Jiang et al., 2018).

110   An image including grayscale rainfall may be mathematically expressed in a two-dimensional (2D) matrix in which each
111   element has a grayscale value. A single image (m×n) is expressed as follows (Jiang et al., 2018):

112    $O = B + R,$ (1)

113   where $O \in R^{m \times n}$, $B \in R^{m \times n}$, and $R \in R^{m \times n}$ are the raw image, rain-free background layer, and rain streak layer.

114   Accordingly, various algorithms are available for rain streak identification. Different still image and video-based algorithms
115   have been proposed to eliminate objects such as moving objects for application to actual surveillance cameras. However, most
116   of these algorithms face optimization problems because of the vast number of decision variables (Jiang et al., 2019). This task
117   is not easy to solve or requires excessive computation time. Therefore, existing studies present techniques suitable for post-
118   analysis rather than application in real-time. The use of complex algorithms can increase versatility and accuracy, but there is
119   a trade-off that reduces computational speed. The time required for such computing is a critical disadvantage in practical
120   applications for estimating rainfall intensity.

121   In this study, a KNN-based segmentation algorithm (Zivkovic and Heijden, 2006), a popular non-parametrical method for
122   background subtraction, was considered for segmenting the rain streaks (foreground) and background layers. KNN is used in
123   classification and regression problems (Bouwmans et al., 2010). The concept of KNN is that similar things are close—the
124   KNN-based segmentation algorithm finds the closest k samples (neighbors) to the unknown sample using Euclidean distance
125   to determine the class (i.e., foreground or background). Thus, the KNN-based segmentation method to detect foreground
126   changes in the video was used to identify rain streaks by recording infrared videos under conditions with little background
127   influence. In the algorithm, The KNN subtractor works by updating the parameters of a Gaussian mixture model for more
128   accurate kernel density estimation (Trnovszký et al., 2017). KNN is more efficient for local density estimation (Qasim et al.,
129   2021); therefore, the algorithm is highly efficient if the number of foreground pixels is low.

130   We used the package provided by OpenCV to implement the KNN-based segmentation algorithm (Zivkovic and Heijden,
131   2006). Accordingly, three main parameters (history, dist2Threshold, detectShadows) needed to be set. Table 1 presents the
132   description of the parameters used for the KNN background subtractor package.

133   **Table 1: Parameters in KNN background subtractor package in OpenCV.**

Parameter	Description

history	Length of the history
dist2Threshold	Threshold on the squared distance between the pixel and the sample to decide whether a pixel is close to that sample. This parameter does not affect the background update.
detectShadows	If true, the algorithm will detect shadows and mark them. This decreases the speed slightly, so if you do not need this feature, set the parameter to false.

134   It is essential to capture raindrops within the camera's depth of field (DoF) to calculate the final DSD and rainfall intensity.

135   Accordingly, this study proposed a novel algorithm to extract each rain streak from the rain streaks image. First, we applied a

136   low-pass filter to the rain streaks image to remove unfocused raindrops that may remain in the image, which smooths each

137   pixel using a 2D kernel. Videos from infrared mode have usually a blur effect. Thus, the additional 2D kernel was applied to

138   remove the pixels having blur. Highly detailed parts (e.g., out-of-focus raindrops and some noises) are erased, leaving some

139   clear rain streaks. A background layer with a value of 0 and a part not in the image were separated to extract the rain streaks

140   and labeled one by one to identify each rain streak from the image.

141   Because the rain streak observed in the surveillance camera image causes an angle difference (influenced by the wind), a

142   diameter estimation process considering the angle of the rain streak (fall angle of a raindrop) is required. If the angle of rain

143   steak is considered and converted to the raindrop diameter through the horizontal pixel size in the image, the shape change in

144   the raindrop because of air buoyancy (i.e., during the falling of the raindrop) may not be reflected, and overestimation can

145   occur.

146   Accordingly, the representative angle of each extracted rain streak was calculated. The border information of each rain

147   streak was obtained, and center axis information of the rain streak was obtained based on the border information to calculate

148   the drop angle. Moreover, the rain streak was rotated to set the long and short axes of the streak at 0° and 90°, using the angle

149   information.

150   The size of raindrops in the rain streaks image can be estimated through the analysis of microphysical characteristics of

151   raindrop and geometric optical analysis (Keating, 2002). The instantaneous velocity of a raindrop on the ground can be

152   estimated from the exposure time and the size of the raindrop. However, the distance from the raindrop to the lens surface (i.e.,

153   the object distance) is unknown and should be inferred. Object distance can be calculated through physical optics analysis

154   because it causes perspective distortion. Assuming a raindrop is spherical, the length of the trajectory where the raindrop falls

155   when the camera is exposed and the diameter of the raindrop can be inferred through the lens equation (Keating, 2002):

156   $L(s) = \frac{d_f - f}{d_f \cdot f} \frac{h_s}{h_p} l_p s,$ (2)

157   $D(s) = \frac{d_f - f}{d_f \cdot f} \frac{w_s}{w_p} d_p s,$ (3)

158   where s is the distance from the raindrop to the lens plane (mm). $L(s)$ and $D(s)$ are the length of falling trajectory during camera

159   exposure (rain streak) and the raindrop's diameter. d_f is the focus distance (mm), f is focal length (mm). h_s and w_s are the

160   vertical and horizontal sizes of the active area of the image sensor (mm), and h_p and w_p are the vertical and horizontal sizes of

161   the captured image (in number of pixels). l_p and d_p are the length and width of the rain streaks in the image (in number of

162   pixels).

163   It is then possible to infer the falling speed of raindrops using the camera's exposure time (Jiang et al., 2019), as follows:

164    $v(s) = \frac{L(s)}{1000\tau},$ (4)

165   where τ is the exposure time of the camera (seconds) and $v(s)$ is the fall velocity of the raindrop from the image. Furthermore,

166   the fall velocity of a raindrop can be approximated by an empirical formula for raindrop diameter. The most frequently used

167   equation is as follows (Atlas et al., 1973; Friedrich et al., 2013):

168    $v(D) = 9.65 - 10.3\exp(-0.6D),$ (5)

169   where D is the raindrop diameter and v is the fall velocity of raindrop. The actual diameter of raindrops can be obtained by

170   solving the equation with the fall velocity obtained through the exposure time and Eqs. (4) and (5). Furthermore, the DoF for

171   the images using the camera's setting information can be calculated, and the effective volume for estimating rainfall intensity

172   can be obtained. Details of the process are described in previous studies (Allamano et al., 2015; Jiang et al., 2019).

173   The control volume must be determined to estimate the rainfall intensity using the diameter of each raindrop. An understanding

174   of DoF is required to achieve the volume. The DoF, is simply the range at which the camera can accurately focus and capture

175   the raindrops. Calculating this range requires obtaining the near and far focus planes as follows:

176    $s_n = \frac{d_f \cdot f^2}{f^2 + N \cdot c_p \cdot (d_f - f)},$ (6)

177    $s_f = \frac{d_f \cdot f^2}{f^2 - N \cdot c_p \cdot (d_f - f)},$ (7)

178   where s_n and s_f are the distances from the near and far focus planes. c_p is the maximum permissible circle of confusion, a

179   constant determined by the camera manufacturers. N is the F-number of the lens relevant to the aperture diameter. Accordingly,

180   the theoretical sampling volume (V, m^3) indicate the truncated rectangular pyramid between the near and far focus planes:

181    $V = \frac{1}{3 \cdot 10^9}\left(\frac{d_f - f}{d_f \cdot f}\right)^2 w_s h_s (s_f^3 - s_n^3),$ (8)

182

183   Then, we used the gamma distribution equation, Eq. (6), proposed by Ulbrich (1983), to calculate DSD parameters using

184   data at every 1 min interval.

185    $N(D) = N_0 D^\mu \exp(-\Lambda D),$ (9)

186   where $N(D)$ (mm^{-1}m^{-3}) is the number concentration value per unit volume for each size channel, and N_0 (mm$^{-1-\mu}$m^{-3}) is an

187   intercept parameter representing the number concentration when the diameter has 0 value. D (mm) and Λ (mm^{-1}) are the drop

188 diameter and slope parameter. Raindrops smaller than 8.0 mm were used to avoid considering non-weather data such as leaps

189 and bugs (Friedrich et al., 2013).

190   The gamma distribution relationship is a function of formulating the number concentration per unit diameter and unit

191 volume. It was proposed by Marshall and Palmer (1948) as improved model of exponential distribution as a favorable form to

192 reflect various rainfall characteristics. By including the term containing μ in the distribution function, the shape of the number

193 concentration distribution for small drops smaller than 1 mm is improved.

194   $N(D) = N_0 \exp(-\Lambda D),$ (10)

195   As the Λ decreases, the slope of the distribution shape decreases and the proportion of large drop increases. Conversely, as

196 the value increases, the distribution slope becomes steeper, and the weight of the large particles decreases. When μ has a large

197 value, the distribution is convex upward, and it has a distribution with a sharp decrease in number concentration at small

198 diameters. Whereas when it has a negative value, the distribution is convex downward with an increase in the concentration

199 of drops smaller than 1 mm. In the gamma distribution, the μ is mainly affected by the difference in concentration of raindrops

200 smaller than 3 mm (Vivekanandan et al., 2004).

201   Vivekanandan et al. (2004) explained the reason for using the gamma distribution as follows. First, it is sufficient to

202 calculate the rainfall estimation equation using only the first, third, and fourth moments (Eq. (11)) (Smith, 2003). Second, the

203 long-term raindrop size distribution has an exponential distribution shape (Yuter and Houze, 1997).

204   The raindrop size distribution observed from the ground is the result of the microphysical development of raindrops falling

205 from precipitation clouds. The drop size distribution shape is changed during fall by microphysical processes such as collision,

206 merging, and evaporation, and changes in the concentration of drops larger than 7.5 mm and small drops occur mainly. As a

207 result, the drop size distribution observed on the ground mainly follows the gamma distribution shape (Ulbrich, 1983; Tokay

208 and Short, 1996). The gamma distribution relationship should be used to analyze the distribution of raindrops that are actually

209 floating and falling.

210   $M_n = \int_{D_{min}}^{D_{max}} D^n N(D) dD,$ (11)

211   Eq. (11) indicate a moment expression for the nth order. For example, the second moment is calculated as the product of

212 the square of the diameter of each channel and the number concentration and the diameter of each channel. Each moment value

213 has a different microphysical meaning. Therefore, the gamma distribution including three dependent parameters is more

214 advantageous in reflecting the microphysical characteristics of the precipitation system than the exponential distribution

215 including two dependent parameters. Eq. (11) can be expressed in gamma distribution format as follows:

216   $M_n = \int_{D_{min}}^{D_{max}} D^n N(D) dD = N_0 \Lambda^{-(\mu+n+1)} \Gamma(\mu + n + 1),$ (12)

217 where N_T (total number concentration, m^{-3}) is the zero-order moment (M_0) and represents the total number concentration of

218 raindrops per unit volume. η was determined for calculating μ and Λ. In this study, a combination of moments in the ratio of

219 M_2, M_4, and M_6, which accurately represents the characteristics of small rainfall particles, was applied (Vivekanandan et al.,

220 2004):

221 $\eta = \frac{\langle M_4 \rangle^2}{\langle M_2 \rangle \langle M_6 \rangle} = \frac{(\mu+3)(\mu+4)}{(\mu+5)(\mu+6)}$, (13)

222 μ and Λ are calculated as follows:

223 $\mu = \frac{(7-11\eta) - \left[(7-11\eta)^2 - 4(\eta-1)(30\eta-12)\right]^{1/2}}{2(\eta-1)}$, (14)

224 $\Lambda = \left[\frac{M_2\Gamma(\mu+5)}{M_4\Gamma(\mu+3)}\right]^{1/2} = \left[\frac{M_2(\mu+4)(\mu+3)}{M_4}\right]^{1/2}$, (15)

225   A larger value of D_m (mm) estimated using Eq. (16), the diameter of the average mass of raindrops contained in the unit

226 volume, indicates that predominantly larger drops are distributed.

227 $D_m = \frac{M_4}{M_3}$, (16)

228   R (mm h^{-1}) is the rain rate calculated using Eq. (17).

229 $R = \frac{6\pi}{10^4} \int_{D_{min}}^{D_{max}} D^3 N(D) V(D) dD$, (17)

3 Study site and observation equipment

231 This study used a building's rooftop as the study site. The building is the Chung-Ang University's Bobst Hall, located in the

232 central region of Seoul in Korea. It is located at 37° 30' 13" north latitude and 126° 57' 27" east longitude, at an elevation of

233 42 m. Fig. 3 illustrates the CCTV (marked with a red circle) and PARSIVEL installed at the study point. The CCTV was used

234 for the main analysis, and PARSIVEL was considered for verification purposes.

(a) Surveillance camera   (b) PARSIVEL

235 **Figure 3: Observation measurements considered in this study.**

236   The CCTV model used in this study is DC-T333CHRX, developed by IDIS. The camera has a 1/1.7 inch complementary

237 metal-oxide semiconductor (CMOS) with a height and width of 5.70 mm and 7.60 mm. The focal length is 4.5 mm, and the

238 F-number of the lens is 1.6. The shutter speed was set to 1/250 s, and the frame per second (fps) was set to 30. The infrared

239 ray distance is 50 m. The maximum permissible circle of confusion is 0.005 mm. The camera's resolution is 1,080 pixels for

240 the height and 1,920 pixels for the width, but the cropped images (640×640 pixels) were considered for the analysis.

241   The PARSIVEL is a ground meteorological instrument that can observe precipitation particles' diameter and fall speed

242 (e.g., raindrops, snow particles, hail). The meteorological information, including raindrop size, is used to estimate the

243 quantitative precipitation amount and reveal the precipitation system's microphysical characteristics and development

244 mechanism.

245   The PARSIVEL used in this study is the second version of the instrument manufactured by OTT in Germany, and it is

246 improved observation accuracy of small particles. The PARSIVEL uses a laser-based optical sensor to send a laser from the

247 transmitter and continuously receive it from the receiver (Fig. 4). As the laser beam moves from the transmitter to the receiver,

248 the precipitation particle passes over the laser beam, and the size and velocity of the precipitation particle are observed (Nemeth

249 and Hahn, 2005). The diameter and velocity of the particle are calculated by calculating the time the particle passes through

250 the laser and the laser intensity that decreases during the passage (Fig. 5).
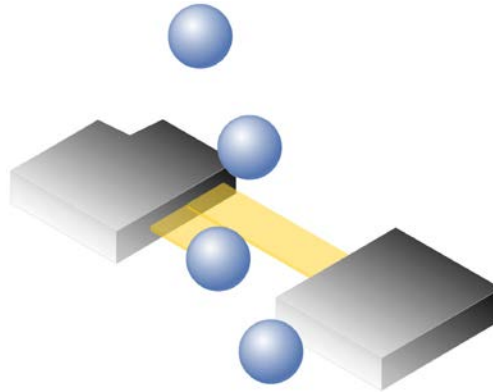
251 **Figure 4: Functional principle of the PARSIVEL disdrometer.**
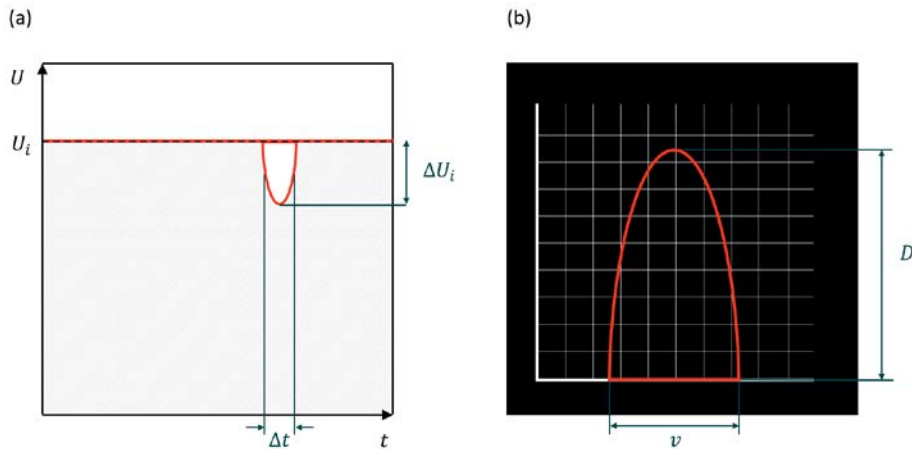
252 **Figure 5: (a) Signal changes whenever a particle falls through the beam anywhere within the measurement area. (b) The degree of**
253 **dimming is a measure of the particle's size; together with the duration of the signal, the fall velocity can be derived.**

254   Parameters such as rain rate, reflectivity, and momentum of raindrops are calculated through particle concentration values

255   for each diameter and falling speed channel obtained through PARSIVEL observation. In this study, the temporal resolution

256   of the observation data was set to 1 minute. The particle diameters from 0.2 to 25 mm (Table 1 in Appendix) and fall velocity

257   from 0.2 to 20 m s^{-1} (Table 2 in Appendix) can be observed by the PARSIVEL. The particle diameter and the fall speed each

258   have 32 observation channels, so the number of observed particles for the time resolution set in 1,024 channels (32×32) is

259   observed. The first and second channels of diameter are not included in the observable range of the PARSIVEL and are treated

260   as noise. Therefore, the observation data of the first and second diameter channels were not considered in the actual analysis.

261   The detailed information on the specifications of the PARSIVEL is presented in Table 2.

262

263   **Table 2: Technical information of the PARSIVEL disdrometer.**

Wavelength of optical sensor		780 nm
Measuring area		30 × 180 mm (54 cm^2)
Measuring range	Size	0.2 ~ 25 mm (32 channel class)
	Fall velocity	0.2 ~ 20 m s^{-1} (32 channel class)
Precipitation intensity		0.001 ~ 1,200 mm h^{-1}
Measurement time interval		10 sec ~ 60 min
Instrument dimensions (H×W×D)		670 × 600 × 114 mm

264

4 Application result

4.1 Rainfall event

We considered two rainfall events from 1945 LST on March 25, 2022, to 0615 LST on March 26, 2022 (case 1), and 2100 LST on September 5, 2022, to 0300 LST on September 5, 2022 (case 2). Fig. 6 illustrates the hyetographs of the rainfall event considered in this study according to the time resolution. The total rainfall of case 1 and 2 is 19.5 and 48.7 mm based on the PARSIVEL, respectively. The maximum rain rate is 10.0 and 20.7 mm h^{-1} based on the 1 min resolution, and 5.0 and 14.5 mm h^{-1} based on the 15 min resolution for case 1 and case 2.

(a) Case 1

(b) Case 2
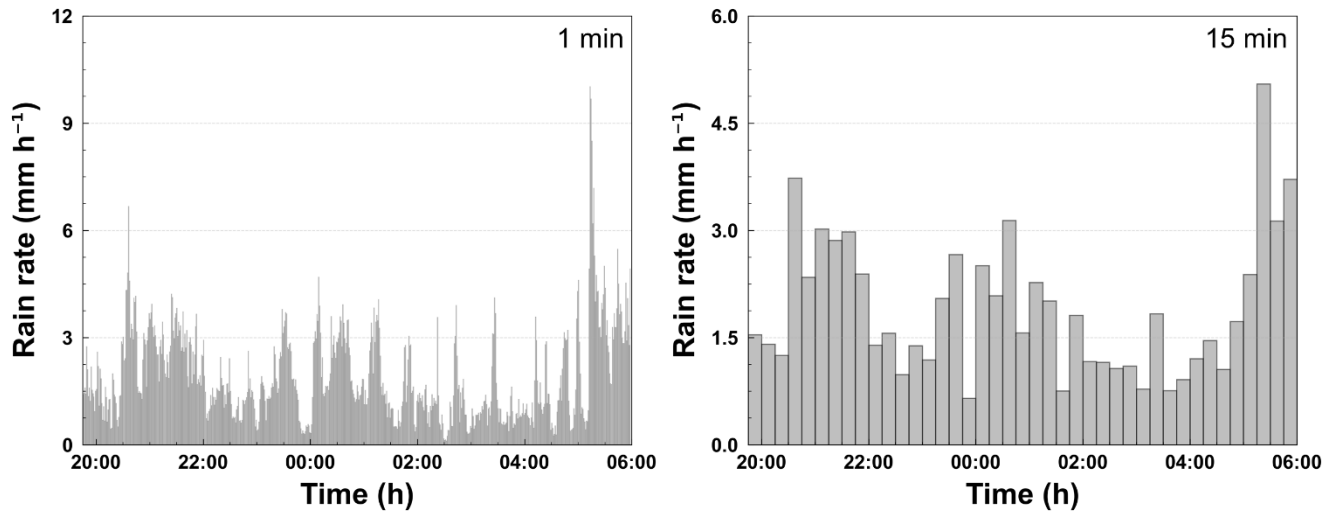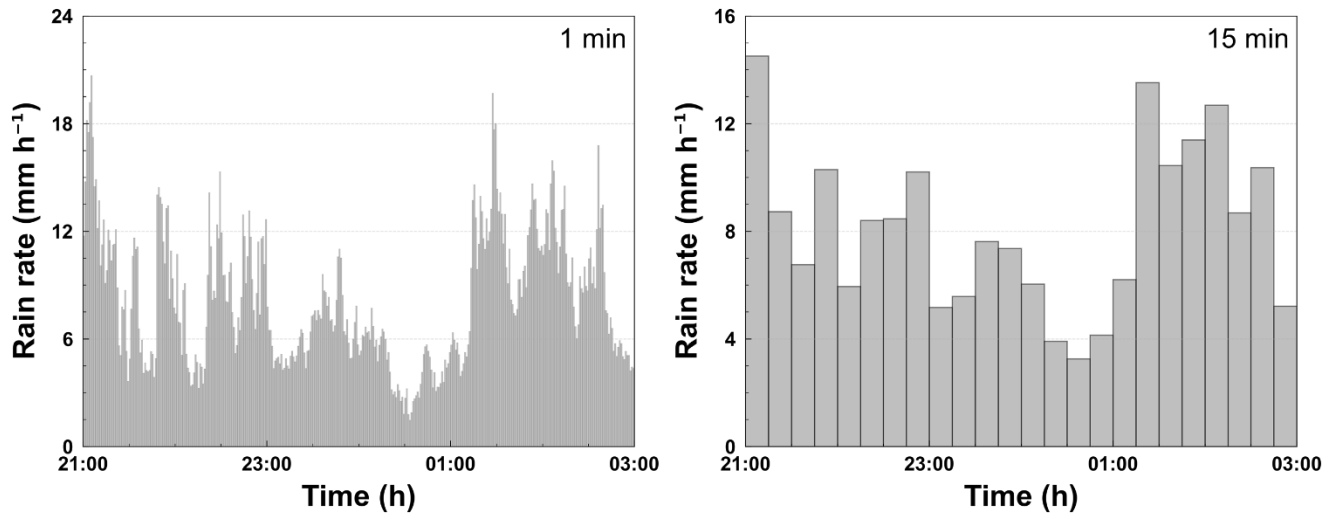
273 Figure 6: Hyetograph of PARSIVEL and rain gauge observation data for the rainfall events considered in this study (left: 1 min
274 resolution, right: 10 min resolution).

275 4.2 Identifying rainfall streaks

276 The rain streaks were distinguished from the original raw images using the KNN-based algorithm described in Section 2.2.

277 Accordingly, two parameters (history and dist2Threshold) were set to default values (500 and 400). The other parameter

278 (detectShadows) was set to "false." Fig. 7 illustrates the raw, background, and rain streaks images for an example time image

279 (20:30:57 March 25, 2022), scaled in yellow to make it easier to verify the visual change.
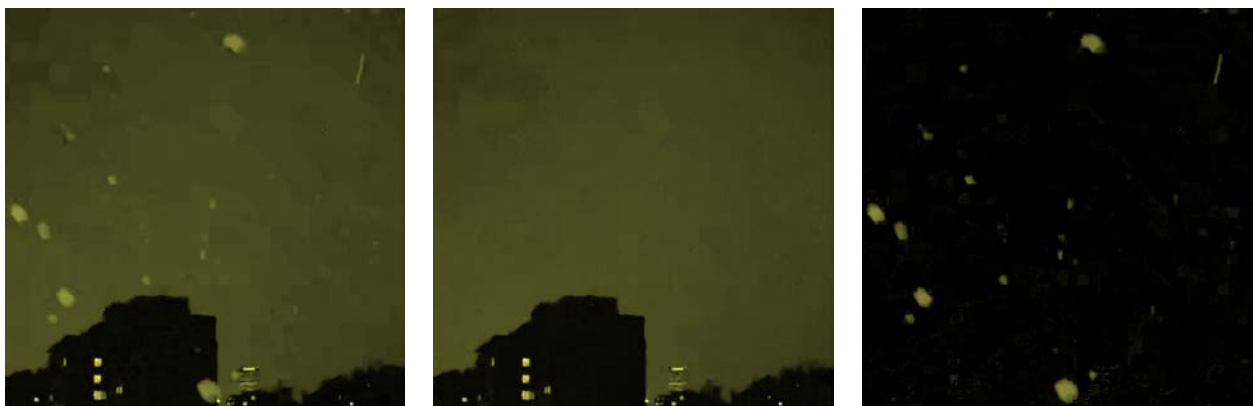
(a) Raw image   (b) Background image   (c) Rain streaks image

280 Figure 7: Segmentation example of raw image into background and rain streaks image based on KNN-based algorithm (20:30:57
281 March 25, 2022).

282   As confirmed in Fig. 7, adequate background separation performance can be achieved using the KNN-based method used

283 in this study. Because it is an infrared camera and the camera's exposure time is 1/250 s, the length of rain streaks is relatively

284 short. The longer the exposure time, the longer the raindrops appear on the image (Schmidt et al., 2012; Allamano et al., 2015).

285 If the exposure time is too long, some rain streaks may penetrate the image. In this case, it is difficult to estimate the rain streak

286 length, a clue for estimating raindrop size.

287   The identification algorithm was implemented using Anaconda Software Distribution on a workstation with an AMD Ryzen

288 5 5600X 6-Core Processor and 32 GB RAM. The computing time for the 15 min video was approximately 50 s using only

289 CPU computation. As described previously, the KNN-based algorithm used in this study has high-speed computing

290 performance compared with various algorithms based on optimization, so it will likely have an advantage in real-time

291 applications.

4.3 Estimation of DSD and rain rate

The rain streaks image presented in Fig. 7(c) was not considered for the final DSD estimation because of noise and factors other than rain caused by the sudden brightness change. As described in Section 3, a low-pass filter was first applied rain streaks image.

The 10×10 kernel was applied considering the total image size (640×640), and each grid value of the kernel was set to 0.01. The set kernel was filtered by convolution pixel by pixel. Moreover, the convolution was performed once more using the following 2D kernel [0 1 0; -1 0 1; 0 -1 0] to highlight the rim of the rain streaks. A background layer with a value of 0 and a part not in the image were separated to extract the rain streaks, which were labeled one by one to identify each rain streak from the image. Fig. 8(a) illustrates the example result after performing the processes described above to Fig. 7(c). Each rain streak was then separated and labeled, as in Fig. 8(b).
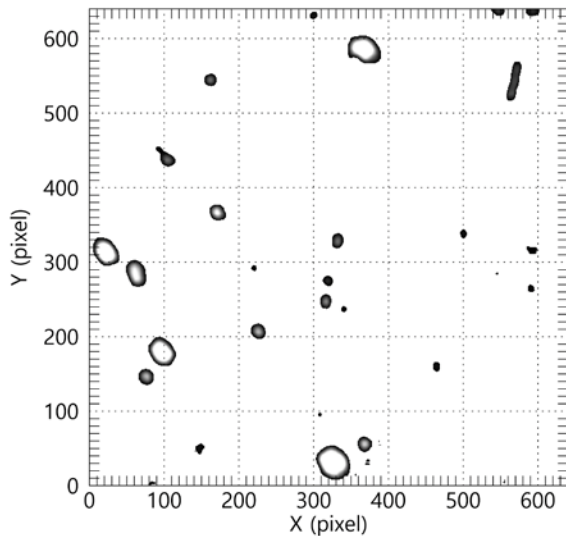
(a) Rain streaks image refined by low-pass filter   (b) Separated and labeled rain streaks
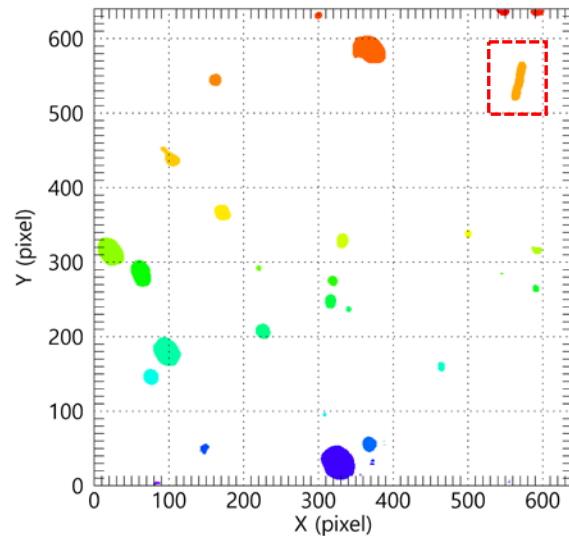
(c) Center axis for a rain streak   (d) Rotated rain streak considering canting angle
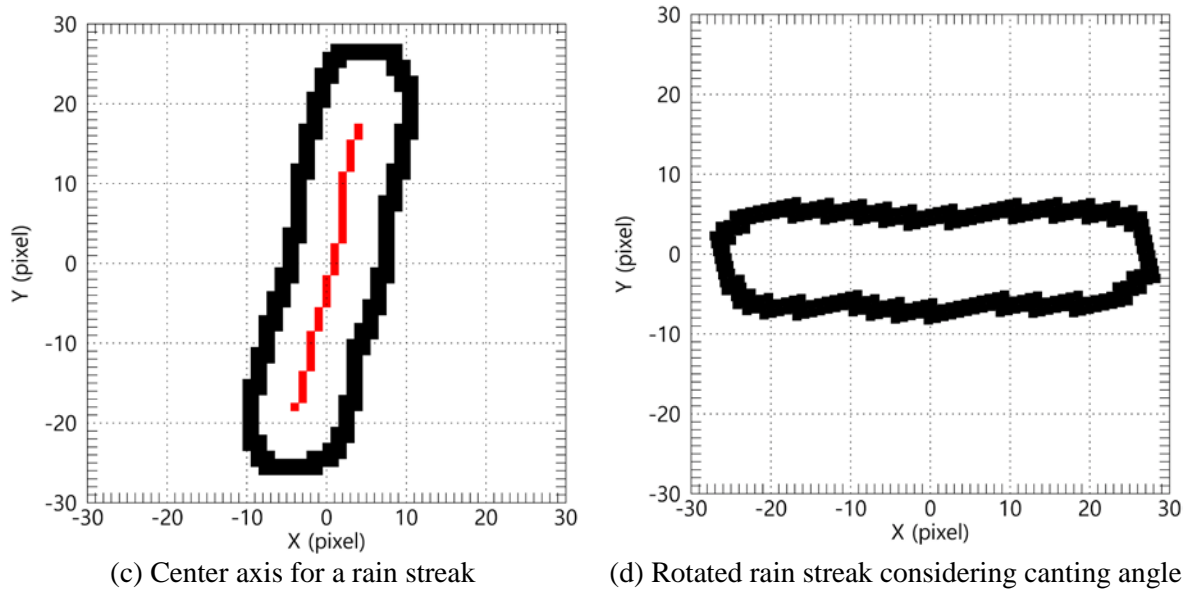
Figure 8. Extraction example of rain streak based on the proposed algorithm.

The border information of each rain streak needed to be obtained. The center axis was calculated by connecting the center (median) of the minimum pixel and maximum pixel values of the x-axis for each y-axis using border information. The angle of rain steak was obtained from the slope value obtained by calculating the linear function through the center axis's x and y pixel number values. Fig. 8(c) is an example of the extraction of a rain streak extracted from the image of Fig. 8(b).

The drop angle was then calculated, and the rain streak was rotated using the angle information. Raindrops can be broken up by strong wind or collisions between raindrops during falling. The maximum difference value between the minimum and maximum pixel number values of y-axis calculated using border information of the rotated rain steak was used to calculate the raindrop diameter and exclude the influence of the distorted shape of rain steak by break up (Fig. 8(d)) (Testik, 2009; Testik and Pei, 2017). Fig. 8(d) illustrates the result of the final process. If the rain streaks overlap, the diameter of the raindrops can be estimated as large. To reduce the overestimation of raindrop diameter, this study tried to find the main central axis coordinates of overlapping rain streaks and set the longest central axis as the representative value. Then, estimate the primary diameter by calculating the distance between each pixel value of the set central axis and the edge pixels of rain streaks.

Fig. 9 illustrates the time series of the number concentration and D_m obtained from CCTV and PARSIVEL. From 1945 LST to 2350 LST, the maximum number concentration of lower than 1,000 $mm^{-1}m^{-3}$ was observed from the PARSIVEL observation, and from 2000 LST to 2010 LST, a number concentration lower than 100 $mm^{-1}m^{-3}$ was observed. At 2005 LST, large raindrops (of 3.8 mm) were observed, resulting in a sharp increase in D_m above 2 mm. In contrast, in the results based on CCTV images, the number concentration of less than 10,000 $mm^{-1}m^{-3}$ was continuously demonstrated during the entire analysis period, and a number concentration greater than 5,000 $mm^{-1}m^{-3}$ was observed before 2200 LST. Because the proportion of small drops was high, D_m was predominantly less than 1.5 mm.

322   From 0000 LST to 0100 LST, both CCTV and PARSIVEL-based data had a predominant maximum diameter of about 2.4

323   mm. At 0035 LST, raindrops larger than 3.2 mm were observed in PARSIVEL, but raindrops less than 3 mm were not observed

324   in CCTV. However, the number concentration of small diameters of 0.5 mm or less had similar values between 1,000 and

325   5,000 $mm^{-1}m^{-3}$. Despite the difference in the maximum size of the drops, there was no predominant difference in the D_m

326   because the number concentration of raindrops smaller than 1 mm had similar values.

327   From 0300 LST to 0530 LST, number concentrations higher than 5,000 $mm^{-1}m^{-3}$ in the raindrops smaller than 1 mm were

328   observed using PARSIVEL. However, CCTV data revealed that number concentrations less than 5,000 $mm^{-1}m^{-3}$ were

329   consistently observed. From 0500 LST to 0510 LST, CCTV image-based number concentration consistently appeared as about

330   1.2 mm, whereas D_m was smaller than 0.7 mm in PARSIVEL. The cause for the rapid decrease in D_m of the PARSIVEL was

331   that the CCTV-based maximum diameter is about 2.4 mm, which was similar to the PARSIVEL observation data, but the

332   number concentration of 0.5 to 0.6 mm raindrops observed by PARSIVEL had a large value of more than 10,000 $mm^{-1}m^{3}$.

333

334
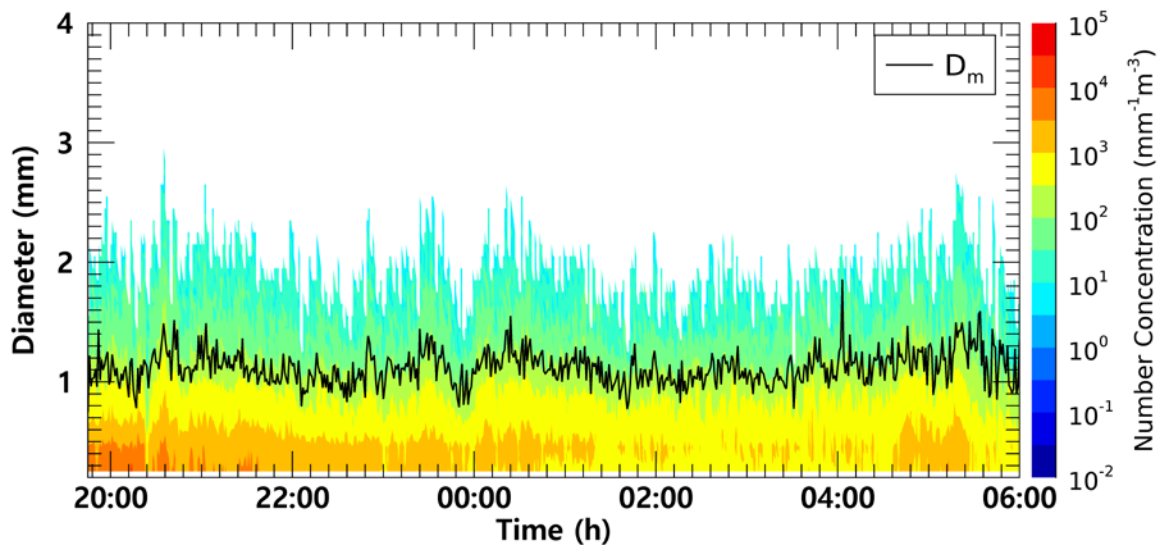
(a) CCTV
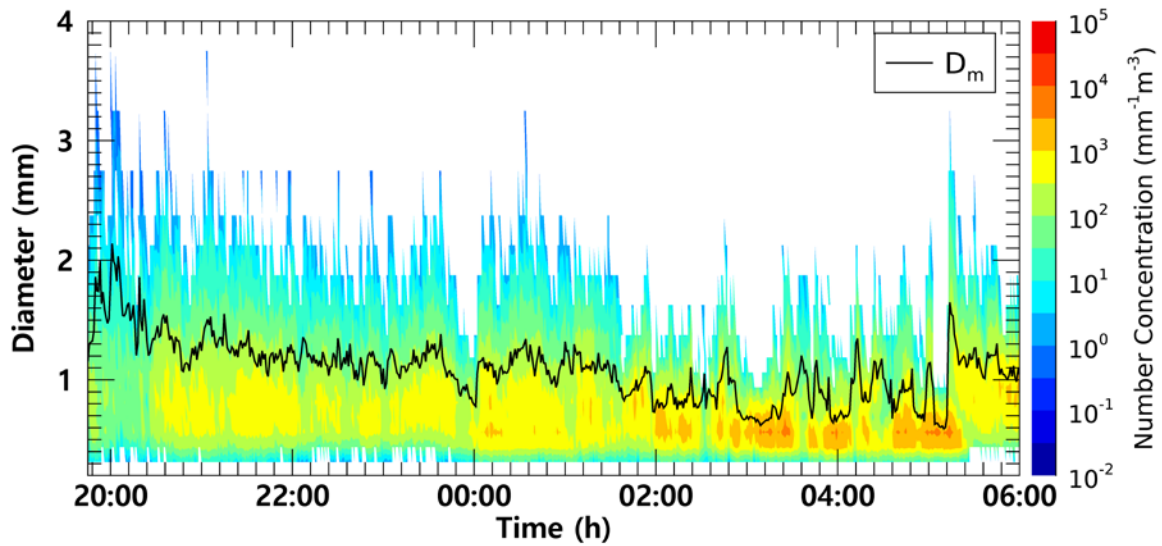
(b) PARSIVEL

Figure 9: Time series of number concentration and Dm (black coloured line) from (a) the surveillance camera images, (b) the PARSIVEL observation data from 2145 LST on March 25 to 0600 LST on March 26, 2022 (case 1).

Fig. 10 illustrates the average number concentration versus diameter of raindrops calculated using CCTV image and PARSIVEL observation data from 1945 LST on March 25 to 0600 LST on March 26, 2022. The PARSIVEL disdrometer data has a fixed raindrop diameter channel; thus, it can differ in number concentration depending on the diameter channel setting. Therefore, in this study, the simulated DSD through the gamma model was also analyzed to compare the distribution of rainfall particles.

For raindrop diameters from 0.7 to 1.5 mm, the simulated and observed number concentrations produced similar values. However, above 1.5 mm, the model-based number concentration was under-simulated. From these results, in the precipitation case selected in this study, the gamma model appears limited in simulating the number concentration of raindrops larger than 3 mm. In diameters from 0.2 to 1.0 mm and above 1.5 mm, the number concentration obtained from CCTV images tended to be higher than that from PARSIVEL observation. PARSIVEL observation data decreased sharply for diameters smaller than 0.3 mm. In contrast, CCTV gradually increased the number concentration as the diameter decreased.
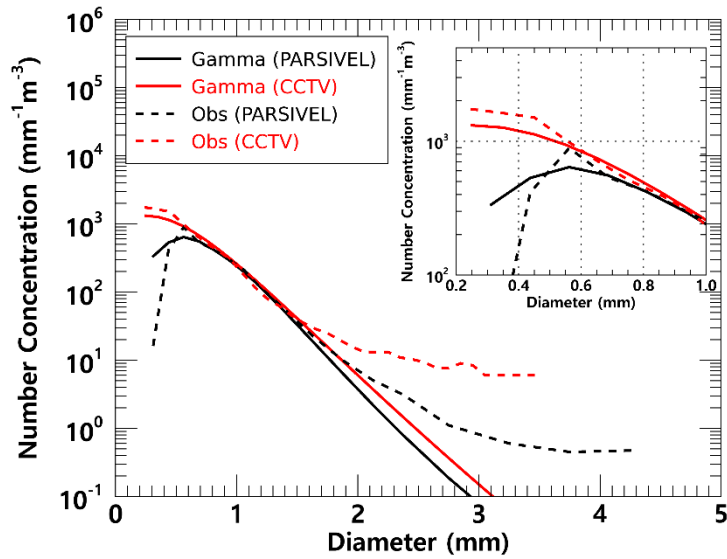
348 **Figure 10: Average number concentration versus diameter from the surveillance camera images and the PARSIVEL (case 1).**

349   Rainfall intensity was estimated based on the obtained number concentration from CCTV images and PARSIVEL. The

350 near (s_n) and far (s_f) focus planes were calculated as 718 and 1,648 mm from Eqs. (8) and (9). The DoF was calculated as 930

351 mm. The focal distance was set to 1 m, referring to previous studies (Dong et al., 2017; Jiang et al., 2019). The control volume

352 was 2.9 m^{-3}, applying Eq. (10) with the variables determined above. Fig. 11 illustrates the rain rate time series calculated using

353 CCTV images and PARSIVEL observation data. The increase or decrease in rain rate according to time change based on

354 CCTV data followed the trend of rainfall intensity change based on PARSIVEL observation data.

355   At 2037 LST, the PARSIVEL based rain rate was 5.9 mm h^{-1}, but the CCTV based rain rate was overestimated to be higher

356 than 10 mm h^{-1}. On the other hand, the CCTV based rain rate was underestimated by about 2 mm h^{-1} than the PARSIVEL

357 based rain rate at 0514 LST. Quantitative changes in CCTV based rain rate showed a similar tendency to increase and decrease

358 the number concentration of raindrops smaller than 1 mm and the maximum diameter. From 0100 LST to 0200 LST, when the

359 number concentrations of CCTV and PARSIVEL had similar values, the rain rate also showed similar results.
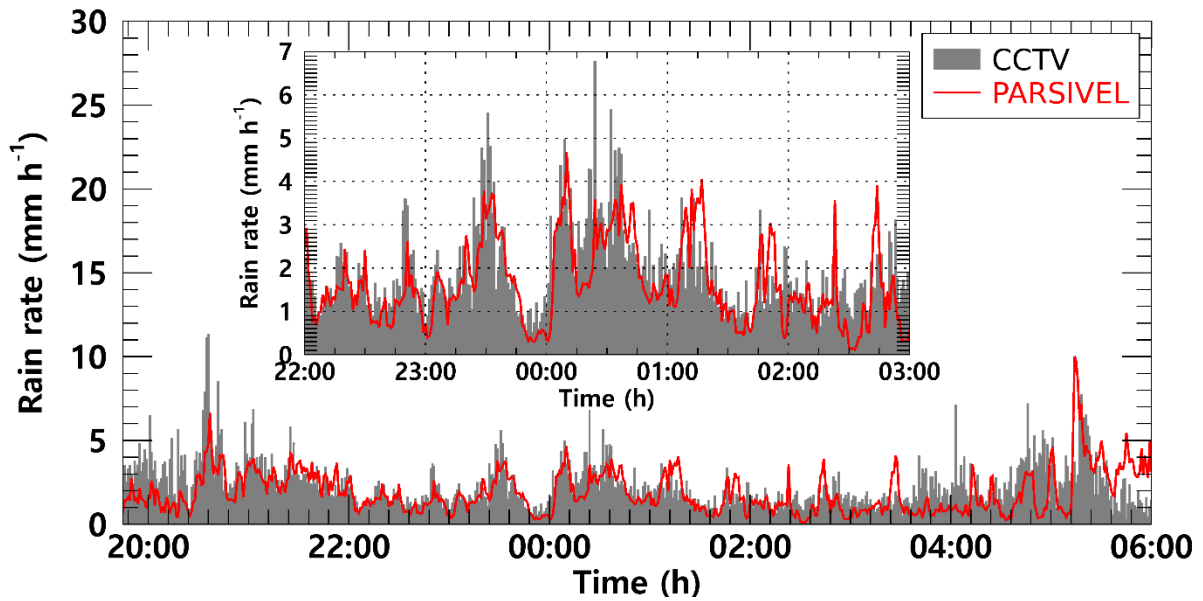
360 **Figure 11: The rain rate time series calculated from the surveillance camera images (gray bar) and PARSIVEL observation data**
361 **(red line) from 2145 LST on March 25 to 0600 LST on March 26, 2022 (case 1).**

362   Fig. 12 illustrates the scatter plot of the average rain rate every 15 min from the PARSIVEL observation and the CCTV

363 images. Uncertainty exists in the resolution of the rain gauge in the 1 min step. Accordingly, the time step for analysis is set

364 to 15 min. The slope of the regression line was 0.71 because the CCTV based rain rate tended to be overestimated at a rain

365 rate of weaker than 2 mm h^{-1}.

366   The cumulative average rainfall intensity every 15 min was weaker than 10 mm h^{-1}, concentrated at a rain rate less than 6

367 mm h^{-1}, so the correlation coefficient (CC) was 0.64. Furthermore, the mean absolute error (MAE), root mean square error

368 (RMSE), and mean absolute percent error (MAPE) were 0.61 mm h^{-1}, 0.99 mm h^{-1}, and 48%. Differences according to rain

369 rate can also be determined. The accuracy is higher at a rain rate smaller than 2 mm h^{-1} as a boundary. The MAE, RMSE, and

370 MAPE were 0.29 mm h^{-1}, 0.72 mm h^{-1}, and 38% for a rain rate of 2 mm h^{-1} or less, and 0.58 mm h^{-1}, 1.17 mm h^{-1}, and 55% for

371 a rain rate above 2 mm h^{-1}.

372   The statistical values of the rain rate and DSD parameters for the rainfall cases analyzed in this study are summarized in

373 Table 3. The rain rate and D_m calculated using CCTV images were 0.459 mm h^{-1} and 0.025 mm more than the values calculated

374 using PARSIVEL observation data on average, respectively. A high rain rate and D_m were caused by overestimating the number

375 concentration for raindrops larger than 1.5 mm confirmed in Fig. 10. The number concentration for the small diameter (less

376 than 0.3 mm) was higher in the CCTV data than in the PARSIVEL data. Due to the high concentration value of the number

377 concentration of raindrops below 0.5 mm and above 2 mm, the CCTV based rain rate had a large value.

378   In the D_m calculated through the PARSIVEL observation data, the concentration change of small drops over time was large,

379 and the variance (0.063 mm) of D_m was large due to the rapid change in number concentration. The variability of the maximum

380 diameter was greater in the PARSIVEL observation data, but the variance of the rain rate was greater in the CCTV data. The
381 large variability of the concentration of raindrops below 3 mm was effected the change in the rain rate. Also, due to the high
382 number concentration of small drops, the skewness of CCTV (1.903) based rain rate had a higher value than that of the
383 PARSIVEL (1.589) based rain rate. The low variability (0.063 mm) of the D_m calculated from CCTV data means that the
384 change in the shape of the raindrop size distribution was small, supported by the low variance of Λ (3.016 mm^{-1}).

385

386 **Table 3: Statistical values of the rain rate and DSD parameters for case 1.**

		R (mm h^{-1})	D_m (mm)	$\log_{10}N_0$ (mm$^{-1-\mu}$m^{-3})	μ (unitless)	Λ (mm^{-1})
PARSIVEL	Mean	1.905	1.091	7.379	7.394	11.829
	Variance	1.667	0.063	15.170	35.975	88.288
	Skewness	1.589	0.551	2.470	2.015	2.714
	Kurtosis	5.189	1.233	7.751	5.132	9.165
CCTV	Mean	2.364	1.116	4.857	2.131	5.713
	Variance	1.998	0.021	0.472	1.680	3.016
	Skewness	1.903	0.536	1.109	0.628	1.151
	Kurtosis	6.073	1.041	2.188	0.739	2.506

387
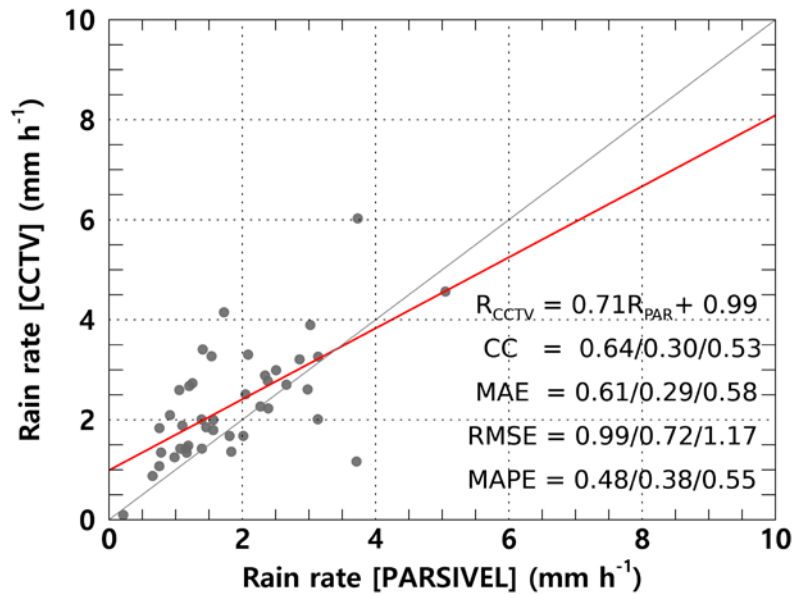
388 **Fig. 12. Scatter plot of average rain rate every 15 minutes from the PARSIVEL observation and the surveillance camera images**
389 **(case 1). Red line is linear regression. Scatter plot displays CC, MAE, RMSE, MAPE for R > 0 mm h^{-1}, R < 2 mm h^{-1}, and R ≥ 2 mm**
390 **h^{-1} (sequentially from left to right).**

391

392   Fig. 13 illustrates the time series of the number concentration and D_m obtained from CCTV and PARSIVEL for case 2. In

393   both CCTV and PARSIVEL observation data, the number concentration for a diameter between 0.5 mm and 1.5 mm had a

394   value between 500 mm^{-1}m^{-3} to 5,000 mm^{-1}m^{-3}, and there was no significant change in the number concentration with time.

395   The maximum diameter also consistently had a value close to about 3 mm, and the D_m was also similar to about 1.5 mm

396   because the maximum diameter and the number concentration of 1 mm intermediate drop had similar values.

397   From 0100 LST to 0230 LST, the maximum particle diameter through CCTV was overestimated, resulting in a large value

398   close to 3.5 mm. As a result, the D_m value increased significantly to more than 2 mm. PARSIVEL data showed a sharp decrease

399   in the number concentration of 1 mm drops at 0030 LST, and an increase in D_m under the influence of the decreased number

400   concentration. However, in the case of CCTV, only raindrops smaller than of 1.5 mm were observed at the time, and there was

401   similar in that D_m was decrease (about 1.1 mm).
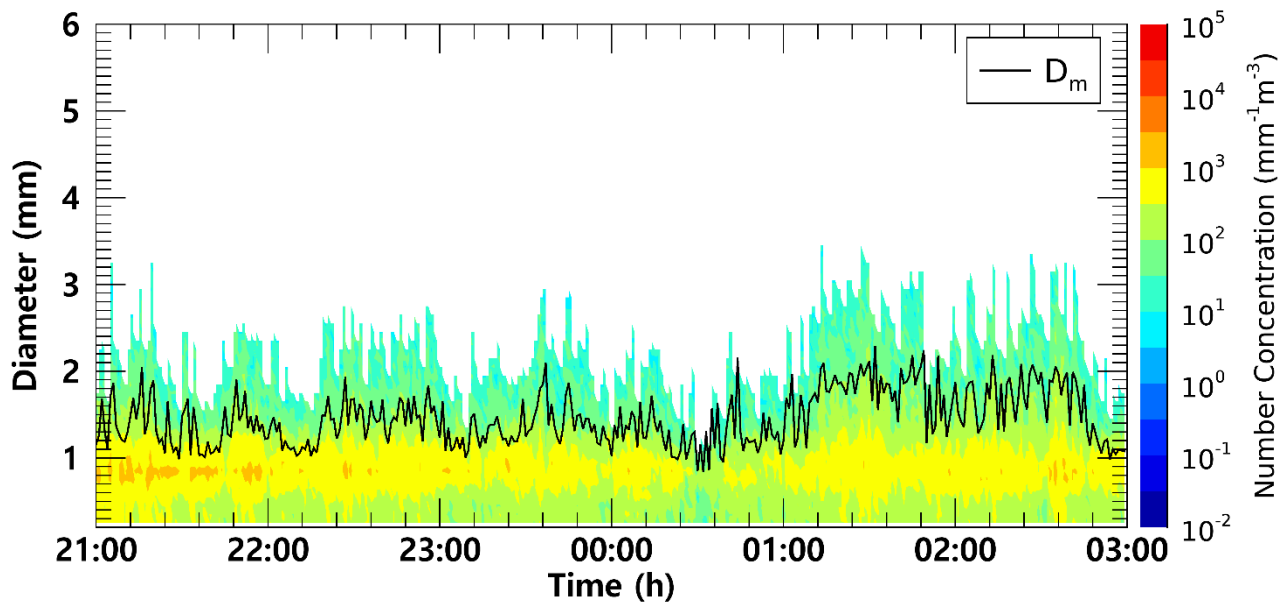
(a) CCTV
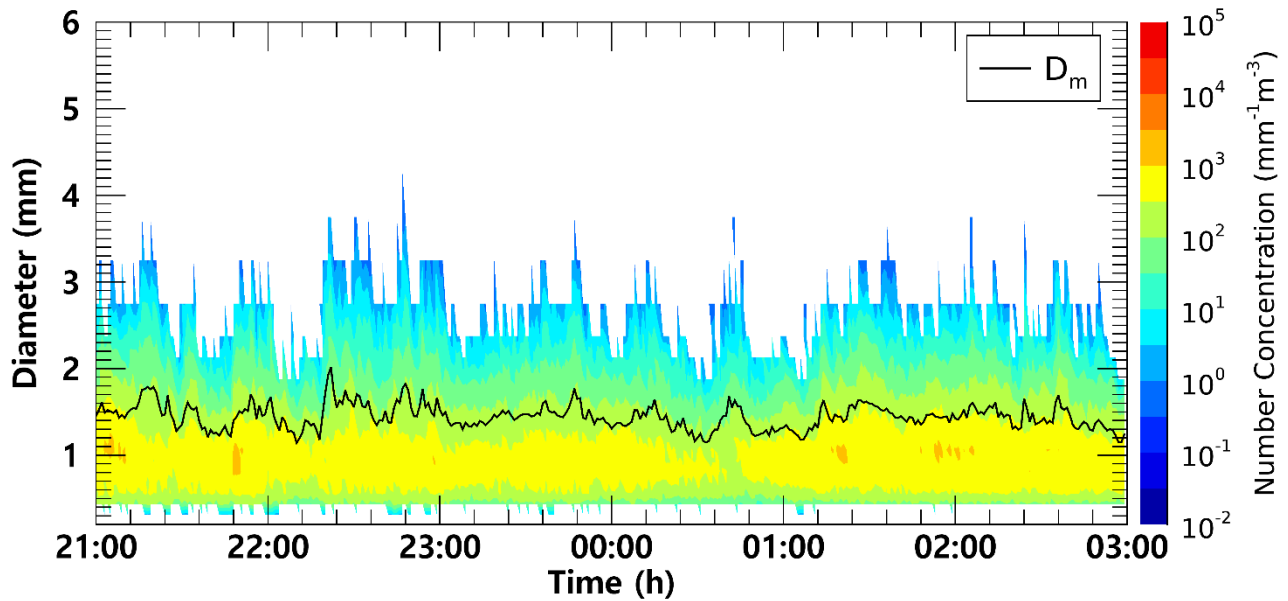
(b) PARSIVEL

Figure 13: Time series of number concentration and D_m (black coloured line) from (a) the surveillance camera images, (b) the PARSIVEL observation data from 2100 LST on September 5 to 0300 LST on September 6, 2022 (case 2).

As clearly shown in Fig. 13, there was no significant difference in number concentration according to the time change. The average number concentration distribution also showed similar results because the number concentration values were concentrated at 1,000 $mm^{-1}m^{-3}$ concentration in both observation instruments. (Fig. 14). As in case 1, PARSIVEL observation data showed a tendency to underestimate in sections less than 0.5 mm and underestimated in sections larger than 2 mm compared to CCTV data. The diameter section where CCTV data is underestimated compared to PARSIVEL data was from 1 mm to 2 mm. Since the number concentration of the CCTV data was underestimated in this section, the rain rate based on the number concentration data was also underestimated compared to the rainfall intensity based on the PARSIVEL data.
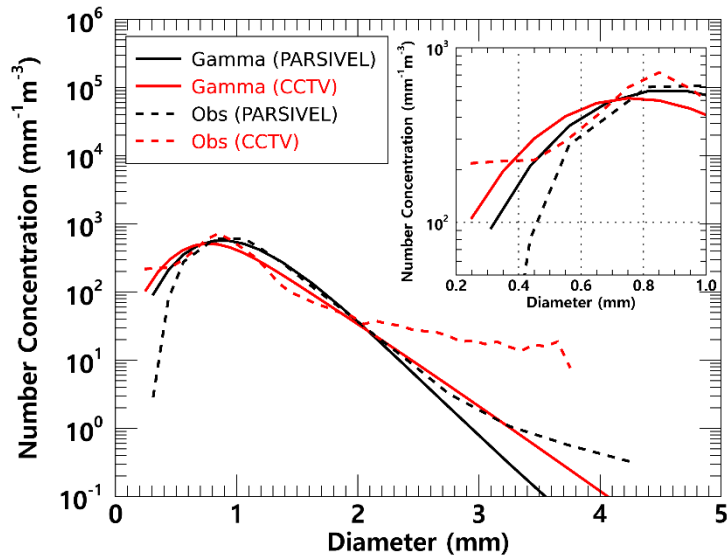
411 **Figure 14: Average number concentration versus diameter from the surveillance camera images and the PARSIVEL (case 2).**

412   Between 2100 LST on September 5 and 0100 LST on September 6, when the number concentration of about 1 mm

413 raindrops is similar and the maximum diameter size is similar, the rain rate time series distribution has a value of about 5 mm

414 h^{-1} and has a very similar flow. However, between 0130 LST and 0300 LST, which is a time period with overestimation of

415 raindrop diameter in CCTV observation data, the increase and decrease in rain rate was similar. However, the magnitude of

416 the increase and decrease rain rate differed every 15 minutes. During that time, the maximum rain rate was less than 20 mm h[-]

417 [1] in the PARSIVEL observation data, while strong rainfall of 30 mm h^{-1} or more was observed in the CCTV observation data.
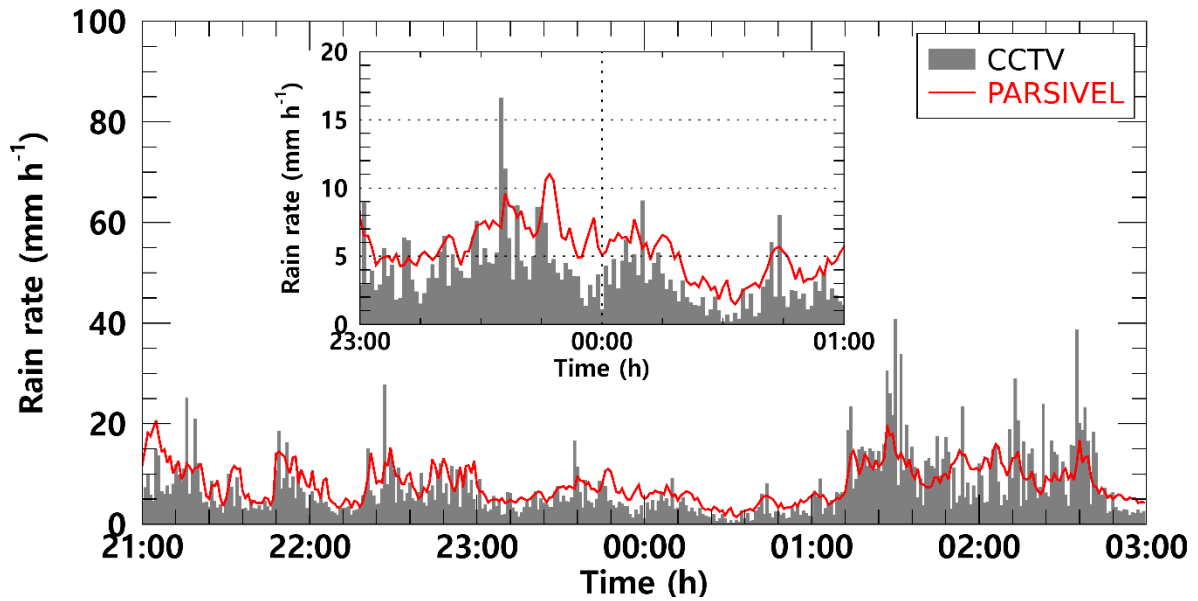
418 **Figure 15: The rain rate time series calculated from the surveillance camera images (gray bar) and PARSIVEL observation data**
419 **(red line) from 2100 LST on September 5 to 0300 LST on September 6, 2022 (case 2).**

420   Fig. 16 illustrates the scatter plot of the average rain rate every 15 min from the PARSIVEL observation and the CCTV

421   images for case 2. Compared to case 1, case 2 was a strong rainfall case with a rain rate of about 8.94 mm h^{-1}. Compared to

422   the PARSIVEL observation data, the CCTV observation data showed a larger D_m by 0.221 mm, while the $Log_{10}N_0$ showed a

423   small feature of 1.1 mm$^{-1-\mu}$m^{-3}. As the weight of medium and large drops over 1 mm increased, μ and Λ showed lower values

424   of 4.262 and 5.397 mm^{-1}, respectively (Table 4). According to the 15-minute cumulative rain rate comparison result, the rain

425   rate based on CCTV image data tends to be underestimated when it is less than 10 mm h^{-1}. Conversely, there was a tendency

426   to overestimate the rainfall period of 10 mm h^{-1} or more. This tendency was confirmed in case 1 which may be caused by

427   recognizing overlapping rain streaks as a single big raindrop. MAPE had a low value of 0.3% or less regardless of the rain rate,

428   and even though the rainfall intensity was relatively large compared to case 1, MAE and RMSE did not significantly increase.

429   This is because there was no abnormally large value of CCTV rainfall during the rainfall period of case 2 compared to case 1.

430 **Table 4: Statistical values of the rain rate and DSD parameters for case 2.**

		R (mm h^{-1})	D_m (mm)	$\log_{10}N_0$ (mm$^{-1-\mu}$m^{-3})	μ (unitless)	Λ (mm^{-1})
PARSIVEL	Mean	8.12	1.445	5.900	6.379	7.341
	Variance	13.82	0.020	1.160	6.498	5.596
	Skewness	0.65	0.447	1.061	0.9467	1.198
	Kurtosis	-0.13	0.472	2.480	1.818	2.792
CCTV	Mean	8.94	1.666	4.813	4.262	5.397
	Variance	69.33	0.121	1.185	4.577	6.714
	Skewness	2.75	0.355	2.596	1.903	2.640
	Kurtosis	11.71	-0.202	8.962	5.714	9.756

431
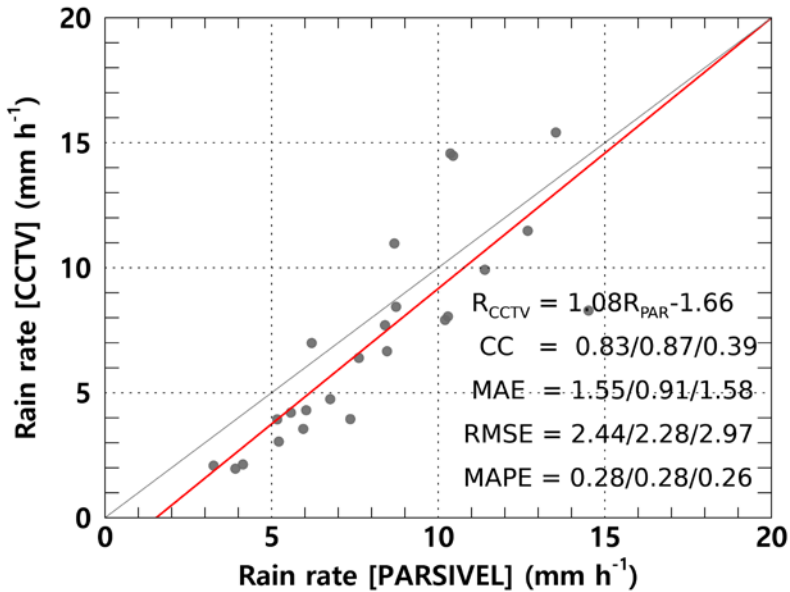
Fig. 16. Scatter plot of average rain rate every 15 minutes from the PARSIVEL observation and the surveillance camera images (case 2). Red line is linear regression. Scatter plot displays CC, MAE, RMSE, MAPE for R > 0 mm h⁻¹, R < 5 mm h⁻¹, and R ≥ 5 mm h⁻¹ (sequentially from left to right).

6 Conclusion

This study estimated DSD with an infrared surveillance camera, based on which rainfall intensity was also estimated. Rain streaks were extracted using a KNN-based algorithm. The rainfall intensity was estimated based on DSD using physical optics analysis. A rainfall event was selected, and the applicability of the method in this study was examined. The estimated DSD was verified using a PARSIVEL. The results from this study can be summarized as follows.

KNN-based algorithm illustrates suitable performance in separating the rain streaks and background layers. Furthermore, the possibility of separation for each rain streak and estimation of DSD was sufficient.

The number concentration of raindrops obtained through the CCTV images was similar to the actual PARSIVEL observed number concentration in the 0.5 to 1.5 mm section. In the small raindrops in the section of 0.4 mm or less, the PARSIVEL observation data underestimates the actual DSD. However, the CCTV image-based rain rate had an advantage over the raindrop-based data—the number concentration decreased rapidly as the number concentration gradually increased in the 0.2–0.3 mm diameter section.

The maximum raindrop diameter and number concentration of less than 1 mm produced similar results during the period with a high ratio of diameters less than 3 mm. However, the number concentration was overestimated during the period when

449 raindrops larger than 3 mm were observed. The CCTV image-based data revealed that the rain rate was overestimated because

450 of the overestimation of raindrops larger than 3 mm. After comparing with the 15-min cumulative PARSIVEL rain rate, the

451 CCs—MAE, RMSE, and MAPE of case 1 (case 2)—were 0.61 mm h^{-1} (1.55 mm h^{-1}), 0.99 mm h^{-1} (1.43 mm h^{-1}), and 48%

452 (44%). The differences according to rain rate can be identified. The accuracy is higher at a rain rate smaller than 10 mm h^{-1} as

453 a boundary.

454 The rain rate and D_m calculated using CCTV images exhibited similar average values. The overestimated number

455 concentration of 1.5 mm or larger caused high kurtosis for the rain rate and D_m of CCTV-based data and a low μ value. Because

456 of the high number concentration for raindrops larger than 3 mm of CCTV, the PARSIVEL observation data had a higher Λ

457 value than the result based on the CCTV data.

458 In this study, DSD was estimated using an infrared surveillance camera; the rain rate was also estimated. Consequently,

459 we could confirm the possibility of estimating an image-based DSD and rain rate obtained based on low-cost equipment in

460 dark conditions. Though, the infrared surveillance camera considered in this study will not be able to replace traditional

461 observation devices, if future studies can be continued to secure robustness, it will be an excellent complement to the existing

462 observation system in terms of spatiotemporal resolution and accuracy improvement.

463 **Appendix. The diameter and fall velocity information for each diameter channel class.**

464 **Table 1: The representative diameter and spread for each diameter channel class.**

Class number	Class average (mm)	Class spread (mm)	Class number	Class average (mm)	Class spread in (mm)
1	0.062	0.125	17	3.250	0.500
2	0.187	0.125	18	3.750	0.500
3	0.312	0.125	19	4.250	0.500
4	0.437	0.125	20	4.750	0.500
5	0.562	0.125	21	5.500	1.000
6	0.687	0.125	22	6.500	1.000
7	0.812	0.125	23	7.500	1.000
8	0.937	0.125	24	8.500	1.000
9	1.062	0.125	25	9.500	1.000
10	1.187	0.125	26	11.000	2.000
11	1.375	0.250	27	13.000	2.000
12	1.625	0.250	28	15.000	2.000
13	1.875	0.250	29	17.000	2.000
14	2.125	0.250	30	19.000	2.000
15	2.375	0.250	31	21.500	3.000
16	2.750	0.500	32	24.500	3.000

465 **Table 2: The representative fall velocity and spread for each diameter channel class.**

Class number	Class average (m s^{-1})	Class spread (m s^{-1})	Class number	Class average (m s^{-1})	Class spread (m s^{-1})
1	0.050	0.100	17	2.600	0.400
2	0.150	0.100	18	3.000	0.400
3	0.250	0.100	19	3.400	0.400
4	0.350	0.100	20	3.800	0.400
5	0.450	0.100	21	4.400	0.800
6	0.550	0.100	22	5.200	0.800
7	0.650	0.100	23	6.000	0.800
8	0.750	0.100	24	6.800	0.800
9	0.850	0.100	25	7.600	0.800
10	0.950	0.100	26	8.800	1.600
11	1.100	0.200	27	10.400	1.600
12	1.300	0.200	28	12.000	1.600
13	1.500	0.200	29	13.600	1.600
14	1.700	0.200	30	15.200	1.600
15	1.900	0.200	31	17.600	3.200
16	2.200	0.400	32	20.800	3.200

Data availability

The data and code can be provided by the corresponding author (hjkim22@cau.ac.kr) upon request.

Acknowledgements

- This research was supported by the Korea Meteorological Administration Research and Development Program (KMI2022-01910) and Basic Science Research Program through the National Research Foundation of Korea (NRF) funded by the Ministry of Education (2022R1I1A1A01065554).

- This research was supported by the Chung-Ang University Graduate Research Scholarship in 2021.

References

Allamano, P., Croci, A., Laio, F.: Toward the camera rain gauge. Water Resour. Res. 51 (3), 1744-1757, 2015

Atlas, D., Srivastava, R. C., Sekhon, R. S.: Doppler radar characteristics of precipitation at vertical incidence. Rev. Geophys. 11 (1), 1–35, 1973.

Avanzato, R., Beritelli, F.: A cnn-based differential image processing approach for rainfall classification. Adv. Sci. Technol. Eng. Syst. J. 5 (4), 438-444, 2020.

479 Bouwmans, T., El Baf, F., Vachon, B.: Statistical background modeling for foreground detection: A survey. In: Chen, C. H.
480 (Ed.) Handbook of pattern recognition and computer vision, fourth ed. World Scientific, Singapore, pp. 181-199, 2010

481 Cai, F., Lu, W., Shi, W., He, S.: A mobile device-based imaging spectrometer for environmental monitoring by attaching a
482 lightweight small module to a commercial digital camera. Sci. Rep. 7 (1), 1-9, 2017.

483 Colli, M., Lanza, L. G., La Barbera, P., Chan, P. W.: Measurement accuracy of weighing and tipping-bucket rainfall intensity
484 gauges under dynamic laboratory testing. Atmos. Res., 144, 186-194, 2014.

485 Deng, L. J., Huang, T. Z., Zhao, X. L., Jiang, T. X.: A directional global sparse model for single image rain removal. Appl.
486 Math. Model. 59, 662.679, 2018.

487 Dong, R., Liao, J., Li, B., Zhou, H., Crookes, D.: Measurements of rainfall rates from videos. In 2017 10th International
488 Congress on Image and Signal Processing, BioMedical Engineering and Informatics, IEEE, Shanghai, China, 14-16 October,
489 pp. 1-9, 2017.

490 Duthon, P., Bernardin, F., Chausse, F., Colomb, M.: Benchmark for the robustness of image features in rainy conditions. Mach.
491 Vis. Appl. 29 (5), 915.927, 2018.

492 Famiglietti, J. S., Cazenave, A., Eicker, A., Reager, J. T., Rodell, M., Velicogna, I.: Satellites provide the big picture. Sci. 349
493 (6249), 684-685, 2015.

494 Friedrich, K., Kalina, E. A., Masters, F. J., Lopez, C. R.: Drop-size distributions in thunderstorms measured by optical
495 disdrometers during VORTEX2. Mon. Weather Rev. 141 (4), 1182-1203, 2013.

496 Garg, K., Nayar, S. K.: Vision and rain. Int. J. Comput. Vis. 75 (1), 3-27, 2007.

497 Guo, B., Han, Q., Chen, H., Shangguan, L., Zhou, Z., Yu, Z.: The emergence of visual crowdsensing: Challenges and
498 opportunities. IEEE Commun. Surv. Tutor. 19 (4), 2526-2543, 2017.

499 Guo, H., Huang, H., Sun, Y. E., Zhang, Y., Chen, S., Huang, L.: Chaac: Real-time and fine-grained rain detection and
500 measurement using smartphones. IEEE Internet Things J. 6 (1), 997-1009, 2019

501 Haberlandt, U., Sester, M.: Areal rainfall estimation using moving cars as rain gauges-A modelling study. Hydrol. Earth Syst.
502 Sci. 14 (7), 1139-1151, 2010.

503 Hua, X. S.: The city brain: Towards real-time search for the real-world. In The 41st International ACM SIGIR Conference on
504 Research & Development in Information Retrieval, New York, NY, 8-12 July. pp. 1343-1344, 2018

505 Jiang, S., Babovic, V., Zheng, Y., Xiong, J.: Advancing opportunistic sensing in hydrology: A novel approach to measuring
506 rainfall with ordinary surveillance cameras. Water Resour. Res. 55 (4), 3004-3027, 2019.

507 Jiang, T. X., Huang, T. Z., Zhao, X. L., Deng, L. J., Wang, Y.: Fastderain: A novel video rain streak removal method using
508 directional gradient priors. IEEE Trans. Image Process. 28 (4), 2089-2102, 2018.

509 Kathiravelu, G., Lucke, T., Nichols, P.: Rain drop measurement techniques: A review. Water, 8 (1), 29, 2016.

510 Keating, M. P.: Geometric, physical, and visual optics, Second ed. Butterworth-Heinemann, Oxford, UK, 2002.

511 Kidd, C., Becker, A., Huffman, G. J., Muller, C. L., Joe, P., Skofronick-Jackson, G., Kirschbaum, D. B.: So, how much of the
512 Earth's surface is covered by rain gauges?. Bull. Am. Meteorol. Soc. 98 (1), 69-78, 2017.

513 Kim, J. H., Sim, J. Y., Kim, C. S.: Video deraining and desnowing using temporal correlation and low-rank matrix completion.

514 IEEE Trans. Image Process., 24 (9), 2658-2670, 2015.

515 Li, Y., Tan, R. T., Guo, X., Lu, J., Brown, M. S.: Rain streak removal using layer priors. In 2016 IEEE Conference on Computer

516 Vision and Pattern Recognition, IEEE, Las Vegas, NV, 27-30 June, pp. 2736-2744, 2016.

517 Löffler–Mang, M., Joss, J.: An optical disdrometer for measuring size and velocity of hydrometeors. J. Atmos. Ocean. Technol.

518 17 (2), 130–139, 2000.

519 Marshall, J. S., Palmer, W. M.: The distribution of raindrops with size. J. Meteor. 5, 165–166, 1948.

520 McCabe, M. F., Rodell, M., Alsdorf, D. E., Miralles, D. G., Uijlenhoet, R., Wagner, W., Lucieer, A., Houborg, R., Verhoest,

521 N. E. C., Franz, T. E., Shi, J., Gao, H., Wood, E. F.: The future of earth observation in hydrology. Hydrol. Earth Syst. Sci. 21

522 (7), 3879-3914, 2017.

523 Michaelides, S., Levizzani, V., Anagnostou, E., Bauer, P., Kasparis, T., Lane, J. E.: Precipitation: Measurement, remote

524 sensing, climatology and modeling. Atmos. Res. 94 (4), 512.533, 2009.

525 Nemeth, K., Hahn, J. M.: Enhanced precipitation identifier and new generation of present weather sensor by OTT Messtechnik,

526 In WMO/CIMO Technical Conference, Germany, 2005.

527 Nottle, A., Harborne, D., Braines, D., Alzantot, M., Quintana-Amate, S., Tomsett, R., Kaplan, L., Srivastava, M. B.,

528 Chakraborty, S., Preece, A.: Distributed opportunistic sensing and fusion for traffic congestion detection. In 2017 IEEE

529 SmartWorld, Ubiquitous Intelligence & Computing, Advanced & Trusted Computed, Scalable Computing & Communications,

530 Cloud & Big Data Computing, Internet of People and Smart City Innovation, IEEE, San Francisco, CA, 4-8 August, pp. 1-6,

531 2017.

532 Overeem, A., Leijnse, H., Uijlenhoet, R.: Two and a half years of country-wide rainfall maps using radio links from commercial

533 cellular telecommunication networks. Water Resour. Res. 52 (10), 8039-8065, 2016.

534 Qasim, S., Khan, K. N., Yu, M., Khan, M. S.: Performance evaluation of background subtraction techniques for video frames.

535 In 2021 International Conference on Artificial Intelligence, IEEE, Islamabad, Pakistan, 5-7 April, pp. 102-107, 2021.

536 Rabiei, E., Haberlandt, U., Sester, M., Fitzner, D.: Rainfall estimation using moving cars as rain gauges–laboratory

537 experiments. Hydrol. Earth Syst. Sci. 17 (11), 4701-4712, 2013.

538 Rabiei, E., Haberlandt, U., Sester, M., Fitzner, D., Wallner, M.: Areal rainfall estimation using moving cars–computer

539 experiments including hydrological modeling. Hydrol. Earth Syst. Sci. 20 (9), 3907-3922, 2016.

540 Santhaseelan, V., Asari, V. K.: Utilizing local phase information to remove rain from video. Int. J. Comput. Vis., 112 (1), 71-

541 89, 2015.

542 Schmidt, J. M., Flatau, P. J., Harasti, P. R., Yates, R. D., Littleton, R., Pritchard, M. S., Fischer, J. M., Fischer, E. J., Kohri,

543 W. J., Vetter, J. R., Richman, S., Baranowski, D. B., Anderson, M. J., Fletcher, E., Lando, D. W.: Radar observations of

544 individual rain drops in the free atmosphere. Proc. Natl. Acad. Sci. 109 (24), 9293-9298, 2012.

545 Smith, P. L.: Raindrop size distributions: Exponential or gamma—Does the difference matter?. J. Appl. Meteorol. Climatol.,

546 42 (7), 1031-1034, 2003.

547 Testik, F. Y.: Outcome regimes of binary raindrop collisions. Atmos. Res. 94 (3), 389–399, 2009.

548 Testik, F. Y., Pei, B.: Wind effects on the shape of raindrop size distribution. J. Hydrometeorol. 18 (5), 1285-1303, 2017.

549 Tokay, A., Short, D. A.: Evidence from tropical raindrop spectra of the origin of rain from stratiform versus convective clouds.
550 J. Appl. Meteorol. Climatol. 35 (3), 355–371, 1996.

551 Tripathi, A. K., Mukhopadhyay, S.: Removal of rain from videos: A review. Signal Image Video Process. 8 (8), 1421-1430,
552 2014.

553 Trnovszký, T., Sýkora, P., Hudec, R.: Comparison of background subtraction methods on near infra-red spectrum video
554 sequences. Procedia Eng., 192, 887-892, 2017.

555 Ulbrich, C. W.: Natural variations in the analytical form of the raindrop size distribution. J. Appl. Meteorol. Climatol. 22 (10),
556 1764–1775, 1983.

557 Vivekanandan, J., Zhang, G., Brandes, E.: Polarimetric radar estimators based on a constrained gamma drop size distribution
558 model. J. Appl. Meteorol. 43 (2), 217-230, 2004.

559 Wang, X., Wang, M., Liu, X., Glade, T., Chen, M., Xie, Y., Yuan, Hao., Chen, Y.: Rainfall observation using surveillance
560 audio. Appl. Acoust. 186, 108478, 2022.

561 Yang, P., Ng, T. L.: Gauging through the crowd: A crowd-sourcing approach to urban rainfall measurement and storm water
562 modeling implications. Water Resour. Res. 53 (11), 9462-9478, 2017.

563 Yuter, S. E., Houze Jr, R. A.: Measurements of raindrop size distributions over the Pacific warm pool and implications for Z–
564 R relations. J. Appl. Meteorol. 36 (7), 847-867, 1997.

565 Zen, R., Arsa, D. M. S., Zhang, R., Er, N. A. S., Bressan, S.: Rainfall estimation from traffic cameras. In: Hartmann, S., Küng,
566 J., Chakravarthy, S., Anderst-Kotsis, G., Tjoa, A., Khalil, I. (Eds.) Database and Expert Systems Applications, Springer, Cham,
567 Switzerland, pp. 18-32, 2019.

568 Zivkovic, Z., Van Der Heijden, F.: Efficient adaptive density estimation per image pixel for the task of background subtraction.
569 Pattern Recognit. Lett. 27 (7), 773-780, 2006.